Domain distributions in tetragonal ferroelectric thin films probed by optical second harmonic generation

Gabriele De Luca [1,2,*] and Manfred Fiebig [1,†]

[1] *Department of Materials, ETH Zurich, Vladimir-Prelog-Weg 4, 8093 Zurich, Switzerland*

[2] *Institut de Ciència de Materials de Barcelona (ICMAB-CSIC), 08193 Bellaterra (Barcelona), Spain*

(Received 23 November 2022; revised 11 July 2023; accepted 3 August 2023; published 17 October 2023)

Controlling the domain arrangement in a ferroelectric material is the key to accessing its functional properties. However, when a ferroelectric thin film is inserted into a multilayer device architecture, conventional characterization techniques provide limited access to the buried distribution of polar states. Here we show that a combination of nondestructive remote probing by nonlinear optics and symmetry analysis allows the unique distinction of the polar orientations coexisting in tetragonal ferroelectric films. We quantify the volumetric ratio between in-plane and out-of-plane polarized domains, and we further illustrate that our approach incorporates the strain-induced changes to the nonlinear susceptibility tensor. We perform the experiment on $Pb(Zr_{0.2}Ti_{0.8})O_3$ thin films, but the generality of the approach permits its extension to other ferroelectric materials.

DOI: 10.1103/PhysRevResearch.5.043055

I. INTRODUCTION

An attractive property of ferroelectric materials is the coexistence of regions with uniform yet different orientations of the polarization, known as domains [1]. Electric-field poling governs their distribution and thus their integrated functional response. Depending on the application, a single-domain state, a multidomain state, or a transformation between the two may be preferred [2,3]. Motivated by the low energy consumption associated with the generation of electric fields, particularly when compared with the energy cost of an electric current driving the generation of a magnetic field, there is great interest in the integration of ferroelectric films into new "green" devices of the oxide-electronics era [4,5]. To reach this goal, the ferroelectric domain structures must be open to proper design, manipulation, and detection. This last step, in particular, unleashes two challenges. First, for engineering a specific ferroelectric domain configuration one has to be able to monitor this configuration, yet without altering it by the probe process. This nonperturbation requirement immediately excludes the use of Sawyer-Tower and positive-up-negative-down circuits and/or inherently destructive techniques like transmission electron microscopy. Second, for a convenient implementation of ferroelectrics in realistic device architectures, their domain configuration needs to be accessible even when buried in a multilayer heterostructure.

Piezoresponse force microscopy (PFM) can access the different domain orientations nondestructively with a resolution of down to ≈ 30 nm, but as a scanning technique it is intrinsically slow and necessitates the presence of a bottom electrode to apply the electric probe field [6,7]. With scanning electron microscopy (SEM), an extreme surface sensitivity and/or surface charging inhibits the access to the interior of the film [8,9]. For both PFM and SEM the ferroelectric layer is often inaccessible when buried beneath a metallic layer. Furthermore, the aforementioned characterization techniques have been developed with the principal aim of imaging domain states with high spatial resolution. Quite often, however, it is the morphology of the domain distribution rather than the explicit shape of the individual domains that controls the functional response of a ferroelectric film [10,11]. In terms of applications, it would therefore be more beneficial to waive some of this essentially unnecessary spatial resolution to get a larger depth sensitivity combined with nondestructive sensing in return.

Here, optical probes can provide a suitable platform, as the penetration depth of the light is only limited by absorption and coherence so that a proper choice of experimental parameters can permit access to the whole volume of a ferroelectric film even when it is buried within a multilayer geometry [12]. The optical resolution is set by the wavelength to the order of 1 μm. In addition to these advantages, the nondestructive and noncontact nature of optical techniques allows us to probe specimens both *in situ*, directly during the film synthesis [13–15], and *operando*, i.e., while applying external stimuli [16–18], two extremely useful features when engineering device functionalities.

Among optical techniques, polarization microscopy builds on the distinction of different domain orientations by birefringence [19,20] which is often unmeasurably small in thin films. Raman spectroscopy is inadequate for working with transparent (ferroelectric) materials if the probe-photon energy is smaller than the band-gap energy [21]. Furthermore, the Raman signal associated with the film is easily obscured by the signal originating in the substrate [22]. In contrast,

*gdeluca@icmab.es

†manfred.fiebig@mat.ethz.ch

Published by the American Physical Society under the terms of the Creative Commons Attribution 4.0 International license. Further distribution of this work must maintain attribution to the author(s) and the published article's title, journal citation, and DOI.

optical second harmonic generation (SHG), that is, frequency doubling of a light wave in a material, is an appropriate technique to characterize ferroelectric thin films [12,23]. Its innate sensitivity to the breaking of inversion symmetry translates directly into a background-free probe of the ferroic state if the substrate itself is, as usual, centrosymmetric.

The development of a model for SHG that incorporates the notion of ferroelectric domains in a crystal dates back to 1964 [24], right after the first laser had been built [25]. Employing SHG to quantify the volumetric ratio of domains in ferroelectric thin films was pioneered by Gopalan and Raj in 1996 [26]. Henceforth, their method has been successfully employed to characterize the domain configurations of $Bi_4Ti_3O_{12}$ [27], $BaTiO_3$ [28], strained $SrTiO_3$ [29], and multiferroic $BiFeO_3$ thin films [30]. This extensive and invaluable work was recently condensed into an open-source code #SHAARP which derives analytical solutions and performs numerical simulations of reflection SHG from a single interface for homogeneous crystals [31]. Still, an open question is how distinct ferroelectric domain configurations within the same material system affect the nonlinear optical signal itself.

Here we show that the SHG response incorporates information on both the volumetric ratio and the arrangement of the ferroelectric domains. To obtain this result, we first derive the nonlinear polarization source term of a tetragonal ferroelectric thin film for both a single-domain and a multidomain configuration. Then, we show that by employing simple symmetry arguments we are able to treat the multidomain configuration as a straightforward extension of the single-domain case. We use this approach to quantify the volumetric amount of out-of-plane- and in-plane-polarized domains in different $Pb(Zr_{0.2}Ti_{0.8})O_3$ (PZT) thin films. Finally, we illustrate how the nonlinear optical response is directly linked to the probed ferroelectric domain architecture. Notably, as our model relies on very general aspects like point-group symmetries and optical interference effects, it can readily be generalized to other classes of ferroelectrics.

The paper is structured in the following way: in Sec. II we present an introduction to SHG in single-domain ferroelectric thin films and its description in terms of the second-order susceptibility $\chi^{(2)}_{ijk}$. In Sec. III we move from single- to multidomain configurations, and we introduce selection rules to model SHG in tetragonal multidomain thin films. In Sec. IV, we use the notion introduced in the preceding sections to develop an explicit but compact form of the nonlinear polarization source term for a generic multidomain case. Finally, in Sec. V we discuss the application of the model to PZT films with qualitatively different domain configurations.

II. SHG IN SINGLE-DOMAIN TETRAGONAL FERROELECTRIC THIN FILMS

In the electric dipole (ED) approximation of the light field [32], SHG is described by the relation

$$P_i(2\omega) = \sum_{jk} \epsilon_0 \chi^{(2)}_{ijk} E_j(\omega) E_k(\omega) \tag{2.1}$$

with indices ijk referring to the axes of a Cartesian coordinate system. An electric radiation field $\boldsymbol{E}(\omega)$ oscillating at a frequency ω impinges onto a material with the nonzero second order susceptibility $\chi^{(2)}_{ijk}$, where it generates a nonlinear polarization $\boldsymbol{P}(2\omega)$. The nonlinear polarization $\boldsymbol{P}(2\omega)$ acts as a source term

$$\boldsymbol{S}(2\omega) \sim \mu_0 \frac{\partial^2}{\partial t^2} \boldsymbol{P}(2\omega) \tag{2.2}$$

in the optical wave equation, promoting the emission of a frequency-doubled radiation field $\boldsymbol{E}(2\omega)$ of intensity $I(2\omega) \sim |\boldsymbol{E}(2\omega)|^2$ from the nonlinear optical medium [33].

This process is phase coherent and parametrized by the coherence length l_c defined as

$$l_c = \frac{\pi}{\Delta \boldsymbol{k}} = \frac{\lambda^{2\omega}}{4(n_{2\omega} \pm n_\omega)}. \tag{2.3}$$

Here $\lambda^{2\omega}$ is the wavelength associated with $\boldsymbol{E}(2\omega)$, and $n_{2\omega}$ and n_ω are the refractive indices of the nonlinear medium at the doubled and fundamental frequencies, respectively. The plus (minus) sign is used in reflection (transmission) geometry. In the following we will focus on the transmission case. Because ferroelectrics are generally transparent in the near-infrared to visible photon-energy range, absorption at ω is usually negligible and typical values of the coherence length are on the order of 1 μm or more. Hence, $\boldsymbol{E}(2\omega)$ is usually generated within the whole volume of the nanoscale ferroelectric film with its typical thickness of $\leqslant$100 nm.

According to the Neumann principle, the nonzero components of the second-order susceptibility $\chi^{(2)}_{ijk}$ are determined by the point-group symmetry of the investigated compound [34]. Hence, the properties and selection rules of the nonlinear polarization $\boldsymbol{P}(2\omega)$ are intimately coupled with the symmetry of the ferroelectric state of our films. Since the ferroelectric order generally breaks the inversion symmetry, all the possible ferroelectric point groups allow for at least one nonzero ED-type $\chi^{(2)}_{ijk}$ component coupling to the spontaneous polarization $\boldsymbol{P}^0$.

In the following we will focus on the case of the technologically most relevant tetragonal ferroelectrics [for instance, perovskitelike $(Ba_{1-x}Sr_x)TiO_3$ [35], $Pb(Zr_{1-x}Ti_x)O_3$ [36], $(K_{1-x}Na_x)NbO_3$ [37], tungsten-bronze-like $(Sr_{1-x}Ba_x)Nb_2O_6$ [38]] with the point-group symmetry 4*mm* in some temperature interval of their phase diagram. We note that a methodological extension of the model to other crystal structures, to domain configurations with a net polarization, or to phase coexistence is straightforward because, although these cases involve different sets of $\chi^{(2)}_{ijk} \neq 0$, the procedures to handle them remain as described in the following. For the 4*mm* point group, the allowed tensor components of $\hat{\chi}^{(2)}$ are tabulated [39] and given by

$$\chi^{(2)}_{zzz}, \quad \chi^{(2)}_{zxx} = \chi^{(2)}_{zyy} \quad \text{and} \quad \chi^{(2)}_{xzx} = \chi^{(2)}_{xxz} = \chi^{(2)}_{yzy} = \chi^{(2)}_{yyz} \tag{2.4}$$

with the x, y, and z directions identified with the [100], [010], and [001] directions of the tetragonal lattice. The [001] direction is conventionally chosen to be the fourfold tetragonal axis and represents the direction of the spontaneous polarization. The nonlinear polarization generating the $\boldsymbol{E}(2\omega)$ radiation is

then given by

$$\boldsymbol{P}(2\omega) \propto \begin{pmatrix} 2\chi^{(2)}_{xxz}E_x(\omega)E_z(\omega) \\ 2\chi^{(2)}_{xxz}E_y(\omega)E_z(\omega) \\ \chi^{(2)}_{zxx}\left[E_x^2(\omega)+E_y^2(\omega)\right]+\chi^{(2)}_{zzz}E_z^2(\omega) \end{pmatrix}. \quad (2.5)$$

Here we have substituted in Eq. (2.1) the tensor components $\chi^{(2)}_{ijk}$ of Eq. (2.4), and $E_x(\omega)$, $E_y(\omega)$, and $E_z(\omega)$ correspond to the components of the electric field of the impinging light oscillating at frequency ω. The measured SHG intensity in the ED approximation is given by the time-averaged field-energy density:

$$I(2\omega) \propto |\boldsymbol{S}(2\omega)|^2 \propto |\boldsymbol{P}(2\omega)|^2 \propto \sum_i |P_i(2\omega)|^2. \quad (2.6)$$

III. $\chi^{(2)}$ SELECTION RULES FOR TETRAGONAL MULTIDOMAIN THIN FILMS

The simplest multidomain configuration involves two domain states of opposite polarization. These form a pair known as 180° domain states. We label these two domain states + and −. As $\hat{\chi}^{(2)} \sim \boldsymbol{P}^0$ [33], we have

$$\chi^{+}_{ijk} = -\chi^{-}_{ijk}, \quad (3.1)$$

where we have dropped the superscript of the $\hat{\chi}^{(2)}$ tensor components for clarity. Because of Eq. (3.1), the SHG light waves associated with the + and – domains exhibit a relative 180° phase shift [40]. Moreover, for a spontaneous polarization $\boldsymbol{P}^0$ formed with respect to a paraelectric cubic structure, there are three equivalent axes leading to six possible tetragonal domain states [41]. Adjacent domains belonging to different pairs of 180° domain states are called 90° domains. In thin films, the out-of-plane-polarized domains are usually known as c domains (along [001]). The in-plane-polarized domains are called a domains with a distinction between a_1 and a_2 domains for a spontaneous polarization pointing along [100] and [010], respectively.

For describing SHG from a multidomain configuration, we express the contributions to the $\hat{\chi}^{(2)}$ tensor in the local coordinate system of each single domain state, and we then transform all of these domain states to the global coordinate system of the crystal for summing up all the domain-specific contributions to $\boldsymbol{P}(2\omega)$. After performing this operation, we get the following allowed tensor components:

$$\chi^{a1}_{xxx}, \quad \chi^{a1}_{xyy} = \chi^{a1}_{xzz} \quad \text{and} \quad \chi^{a1}_{yyx} = \chi^{a1}_{yxy} = \chi^{a1}_{zzx} = \chi^{a1}_{zxz}, \quad (3.2)$$

$$\chi^{a2}_{yyy}, \quad \chi^{a2}_{yzz} = \chi^{a2}_{yxx} \quad \text{and} \quad \chi^{a2}_{zzy} = \chi^{a2}_{zyz} = \chi^{a2}_{xxy} = \chi^{a2}_{xyx}, \quad (3.3)$$

$$\chi^{c}_{zzz}, \quad \chi^{c}_{zxx} = \chi^{c}_{zyy} \quad \text{and} \quad \chi^{c}_{xxz} = \chi^{c}_{xzx} = \chi^{c}_{yyz} = \chi^{c}_{yzy}. \quad (3.4)$$

The a_1, a_2, and c superscripts refer to the respective 180° domain pair. By substituting Eqs. (3.2)–(3.4) into Eq. (2.1) we can derive the total nonlinear polarization $\boldsymbol{P}(2\omega)$ associated to a specific distribution of a_1, a_2, and c domains in the global coordinate system.

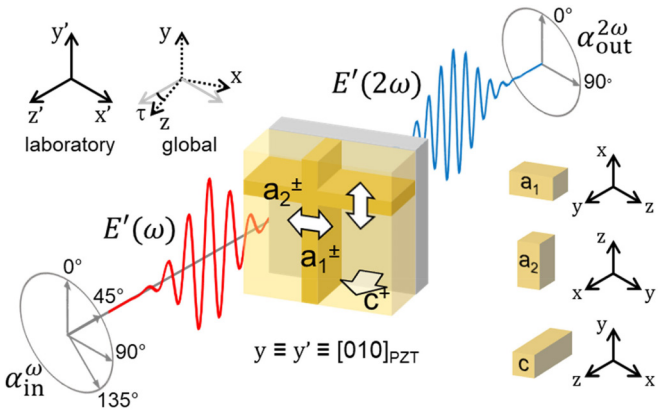

FIG. 1. Schematic of the transmission geometry used to collect the SHG data. The laboratory and global reference systems are depicted in the top-left part of the figure. The local reference system of each domain pair is shown in the right part of the figure. The sample-rotation axis along $y = y'$ is parallel to $[010]_{PZT}$. By rotating the sample by an angle τ, we project both the $[001]_{PZT}$ and $[100]_{PZT}$ onto the x' axis. The possible tetragonal ferroelectric domains in the sample are indicated in yellow in the figure, with the white arrows indicating the polarization orientation. For simplicity, c^- domains are not considered. The polarization angles of the incoming (0°, 45°, 90°, 135°; in red, at frequency ω) and outgoing light (0°, 90°; in blue, at frequency 2ω) determine the $\alpha^{\omega}_{in}/\alpha^{2\omega}_{out}$ configuration. These angles are defined to be 0° when the polarization is parallel to the y' axis.

IV. FERROELECTRIC DOMAIN DISTRIBUTIONS PROBED BY SHG

For comprehensive probing of the ferroelectric state we need to address all three crystallographic directions with our optical excitation. Because of the transversally polarized nature of light, this is accomplished by tilting the sample to obtain an angle τ between its c axis and the $\boldsymbol{k}$ vector of the incoming light. The rotation of the crystal is such that the global coordinate system and the laboratory coordinate system (indicated with a prime) only coincide when $\tau = 0°$. A schematic of this transmission geometry, with xz chosen as the plane of incidence and reflection, is represented in Fig. 1. Analyzing the SHG response in this geometry will be particularly useful in all the cases when the sample can only be accessed remotely [13] and/or when it cannot be rotated around its azimuthal plane. For the electric field of the incident light with $\boldsymbol{k}' \parallel z'$ this yields

$$\boldsymbol{E} = (E'_x \cos\tau,\ E'_y,\ -E'_x \sin\tau). \quad (4.1)$$

Substituting Eq. (4.1) into Eq. (2.5) gives an expression for the nonlinear polarization $\boldsymbol{P}(2\omega)$ in the global coordinate system of the crystal for an arbitrary angle τ. However, it is more convenient to express the nonlinear polarization in the laboratory coordinate system [42]:

$$\boldsymbol{P}'(2\omega) \propto \begin{pmatrix} P_x\cos\tau - P_z\sin\tau \\ P_y \\ P_x\sin\tau + P_z\cos\tau \end{pmatrix}. \quad (4.2)$$

In general, the nonlinear polarization has nonzero components along all three principal axes. However, as only transversally polarized light can leave the crystal, the longitudinal component $P_x \sin\tau + P_z \cos\tau$ will not be considered further. With the aid of Eqs. (3.4), (4.1), and (4.2), we derive $\boldsymbol{E}'(2\omega)$ in the laboratory coordinate system for a single-domain sample with out-of-plane-oriented spontaneous polarization $\boldsymbol{P}^0$. This leads to

$$\begin{aligned} E'_x(2\omega) \propto\ & 2\chi^c_{xxz}(E'_x\cos\tau)(-E'_x\sin\tau)\cos\tau \\ & -\{\chi^c_{zxx}[(E'_x\cos\tau)^2+(E'_y)^2] \\ & +\chi^c_{zzz}(-E'_x\sin\tau)^2\}\sin\tau, \end{aligned} \tag{4.3}$$

$$E'_y(2\omega) \propto 2\chi^c_{xxz}E'_y(-E'_x\sin\tau). \tag{4.4}$$

Note that for $\tau = 0^\circ$ the SHG intensity is zero as requested by the z component in all nonlinear susceptibilities $\chi^c_{ijk} \neq 0$. Hence, c domains will not produce any detectable SHG light in normal incidence [12,43]. Here we are ignoring birefringence-induced phase shifts [23], which are negligible for ultrathin PZT films [44], as discussed in the next section.

For a multidomain sample consisting of a_1, a_2, and c domains, we consider the case where the average domain size is smaller than the lateral optical resolution. For thin films this is a reasonable assumption because according to the Mitsui-Furuichi-Kittel law a ferroelectric film around 100 nm thick translates into an average domain size on the order of 10–50 nm [45], well below the lateral optical resolution. In this case, the second harmonic radiation $\boldsymbol{E}'(2\omega)$ will result from the interference between the nonlinear source terms that are generated locally in the different domains [23]. For an arbitrary distribution of a_1, a_2, and c domains, Eqs. (4.3) and (4.4) for the c-domain case thus expand into

$$\begin{aligned} E'_x(2\omega) \propto\ & \cos\tau\{\delta A^{a1}[\chi^{a1}_{xxx}(E'_x\cos\tau)^2+\chi^{a1}_{xyy}[(E'_y)^2+(-E'_x\sin\tau)^2]]+\delta A^{a2}2\chi^{a2}_{xxy}(E'_x\cos\tau)(E'_y) \\ & +\delta A^c 2\chi^c_{xxz}(E'_x\cos\tau)(-E'_x\sin\tau)\}-\sin\tau\{\delta A^{a1}2\chi^{a1}_{zzx}(E'_x\cos\tau)(-E'_x\sin\tau) \\ & +\delta A^{a2}2\chi^{a2}_{zzy}(-E'_x\sin\tau)(E'_y)+\delta A^c[\chi^c_{zzz}(-E'_x\sin\tau)^2+\chi^c_{zxx}(E'_x\cos\tau)^2+(E'_y)^2]\}, \end{aligned} \tag{4.5}$$

$$E'_y(2\omega) \propto \delta A^{a1}2\chi^{a1}_{yyx}(E'_x\cos\tau)(E'_y)+\delta A^{a2}\{\chi^{a2}_{yyy}(E'_y)^2+\chi^{a2}_{yzz}[(-E'_x\sin\tau)^2+(E'_x\cos\tau)^2]+2\chi^c_{yyz}(E'_y)(-E'_x\sin\tau)\}, \tag{4.6}$$

where we have introduced the quantities

$$\delta A^\nu = A^{\nu+} - A^{\nu-}, \quad \nu = a_1, a_2, c. \tag{4.7}$$

$A^{\nu\pm}$ is the area fraction of the domain variant ν for the respective pair of 180° domain states with $\pm\boldsymbol{P}^0_\nu$ such that $\sum_\nu A^{\nu\pm} = 1$ [23]. The values δA^ν represent, instead, the domain imbalance within every domain pair a_1, a_2, and c. These quantities are identically equal to $A^{\nu\pm}$ when only one domain state of the domain variant ν is present. Note that for normal incidence ($\tau = 0^\circ$) only the a domains contribute to SHG, which clearly distinguishes them from the c domains [43].

Finally, it is convenient to define the angle α as the angle between the light polarization and the y axis (see Fig. 1). In this case, Eq. (4.1) can be rewritten as

$$\boldsymbol{E} \propto (\sin\alpha\cos\tau, \cos\alpha, -\sin\alpha\sin\tau). \tag{4.8}$$

Substituting Eq. (4.8) in place of Eq. (4.1) will result in a modified expression for Eqs. (4.3)–(4.6) that depends only on angular coordinates and the $\hat{\chi}^{(2)}$ tensor components of Eqs. (3.2)–(3.4).

V. EXPERIMENTAL RESULTS AND DISCUSSION

SHG measurements are performed with an amplified Ti:sapphire-laser/optical-parametric-amplifier system emitting 130-fs pulses with a repetition rate of 1 kHz at a fundamental wavelength of 1300 nm (≈0.95 eV). The polarization of the incoming fundamental light beam is rotated using a half-wave plate (polarizer). The polarization of the detected SHG light is selected with a Glan-Taylor prism (analyzer). The SHG light is separated from the fundamental beam using bandpass filters and an optical monochromator. The SHG intensity is collected using a photomultiplier tube and normalized to the grating efficiency of the monochromator.

A key piece of information that can be extracted from Eqs. (4.5) and (4.6) is the domain-pair imbalance (δA^{a1}, δA^{a2}, and δA^c) in a multidomain sample. To access these quantities, ideally, we need to correlate the macroscopic SHG response of a single-domain configuration with the material-specific values of the $\hat{\chi}^{(2)}$ tensor components. Here we show this exemplarily for PZT, the technologically most important ferroelectric. To produce ferroelectric thin films with specific domain distributions, we employ epitaxial strain in PZT films grown on (110)-oriented $DyScO_3$ (DSO) [43,46]. We refer to two distinct samples: a fully strained 15-nm-thick film featuring a single-c-domain configuration and a partially relaxed 75-nm-thick film characterized by stripe-shaped a domains immersed in a c-domain matrix (see Fig. 2). Details on the growth method and the structural and electrical characterization of the films are discussed in Ref. [43].

To evaluate the magnitude of the $\hat{\chi}^{(2)}$ tensor components we concentrate first on the purely c-oriented PZT film. We select the polarization of the incoming light such that $\boldsymbol{E}'(\omega)$ is directed along the four high-symmetry directions of the tetragonal unit cell ($\alpha = 0^\circ$, 45°, 90°, and 135°). We thus obtain a total of eight nontrivial incoming/outgoing light-polarization configurations $\boldsymbol{E}'(\omega)/\boldsymbol{E}'(2\omega)$ with $\alpha^\omega_{\text{in}}/\alpha^{2\omega}_{\text{out}}$ as $0^\circ/0^\circ$, $45^\circ/0^\circ$, $90^\circ/0^\circ$, $135^\circ/0^\circ$, $0^\circ/90^\circ$, $45^\circ/90^\circ$, $90^\circ/90^\circ$, $135^\circ/90^\circ$ that we record as a function of the tilt angle τ, as in Fig. 1. For the data of the single-c-domain PZT sample in Fig. 3 we thus determine the value of the χ^c_{ijk} tensor-component ratios. We do this by *simultaneously* fitting these eight data sets to Eqs. (4.3) and (4.4) under the assumption that the χ^c_{ijk} tensor

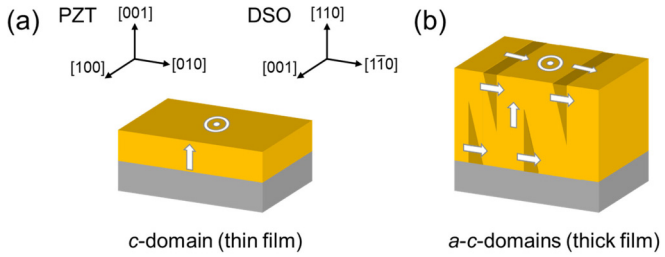

FIG. 2. Strain-engineered domain distribution. (a) A PZT film of 15 nm grown on (110)-oriented DSO exhibits a single-domain configuration with its c axis oriented out of plane. The coordinate systems indicate the epitaxial relation between PZT and DSO. (b) A PZT film of 75 nm results in a a-c domain configuration. The in-plane a domains are predominantly oriented along $[001]_{\mathrm{DSO}}$ as documented by the PFM analysis shown in Ref. [43]. We disregard the most general case with the coexistence of substantial fractions of a_1-a_2-c domains as this is not experimentally observed.

components are real quantities. This assumption is justified by the off-resonance nature of the SHG process whose photon energy (1.9 eV) lies well below the band gap of PZT (≈ 3.5 eV) [48]. From this fit procedure for the single-c-domain PZT film (Fig. 3), we obtain the ratios between the three independent components of χ^c_{ijk} contributing to Eq. (3.4). We find $\chi^c_{zxx}/\chi^c_{zzz} = 0.11 \pm 0.01$ and $\chi^c_{xzx}/\chi^c_{zzz} = 0.20 \pm 0.01$ (Table I). Note that the magnitude of the $\hat{\chi}^{(2)}$ tensor components is affected by multiple reflection via the Fresnel coefficients [47,49], so in principle an angle-dependent correction for the measured second-harmonic intensity needs to be introduced [50]. In our case, however, this is not necessary. First, the enhancement of the second-harmonic power due to multireflection would increase with increasing angle τ and thus lead to a deviation from the parabolic τ dependence in Figs. 3 and 4 [47]. We do not see such a deviation, so we conclude that in our experiment multireflection contributions are negligible. Second, the SHG data are normalized for each sample, and we are fitting the ratios of $\chi^{(2)}$ components rather than their absolute values. This normalization procedure cancels out part of the multireflection effect as it affects all the τ-dependent SHG measurements in a similar way [31,51]. Further, by neglecting the $\cos\delta$ phase factor [$\delta = (\frac{2\pi}{\lambda})\Delta n t$] due to birefringence [23], we are obtaining an upper error limit of 0.1% for the case $\Delta n = 0.1$ [44] and $t = 15$ nm. Comparing this with the error we obtain on the tensor-component ratios (Table I), this systematic error is unimportant. Finally, when using Eqs. (4.5) and (4.6) to estimate the contribution from the a domains we find that it is negligibly small in line with the absence of in-plane-polarized domains in the fully strained PZT film [43].

Within this framework, we can now determine the fraction of stripe-shaped a domains immersed in the c-domain matrix

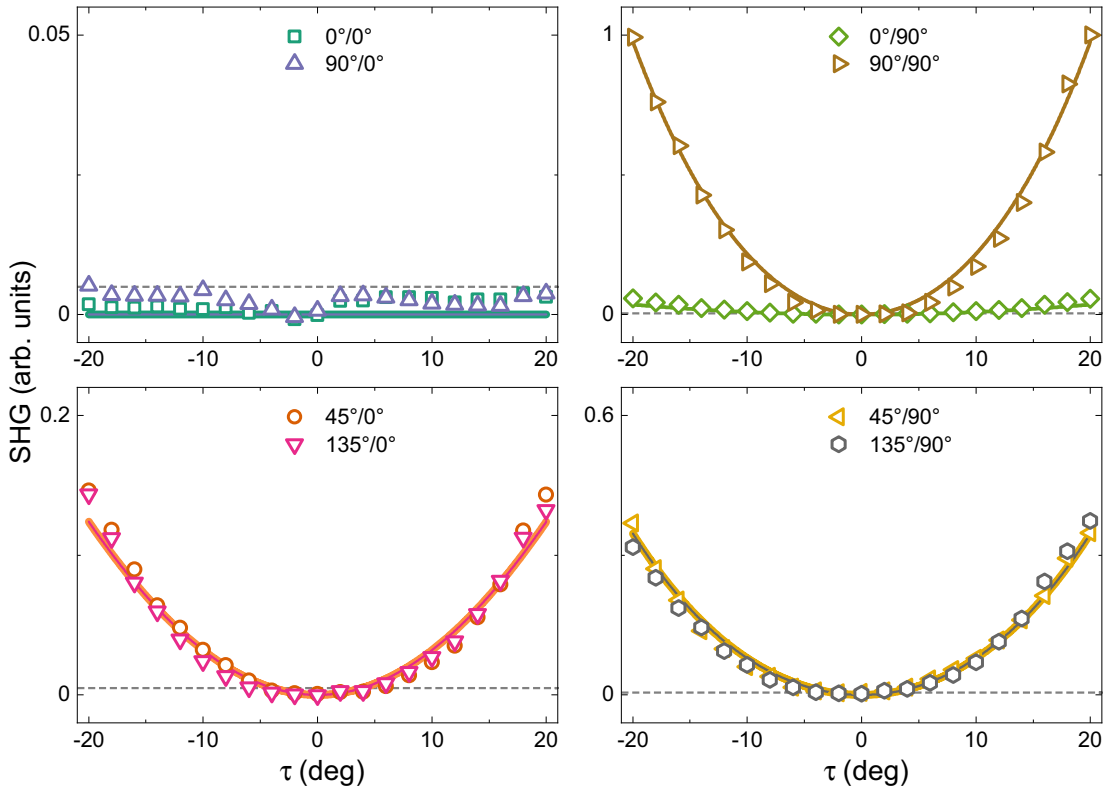

FIG. 3. SHG intensity for different polarization configurations for the single-c-domain PZT film, using the labeling introduced in Fig. 1, is shown as a function of the sample-rotation angle τ. The data are grouped such that the $\alpha^{\omega}_{\mathrm{in}}/0^\circ$ and $\alpha^{\omega}_{\mathrm{in}}/90^\circ$ configurations are shown in the left and right column, respectively. The top (bottom) row is characterized by $\alpha^{\omega}_{\mathrm{in}} = 0^\circ, 90^\circ$ ($\alpha^{\omega}_{\mathrm{in}} = 45^\circ, 135^\circ$). Data are normalized to the $90^\circ/90^\circ$ configuration at $\tau = 20^\circ$. The dashed lines indicate the instrumental background. Continuous lines correspond to the fit model of Eqs. (4.5) and (4.6) with all data fitted with one set of parameters (Table I). Note that all eight fit lines vanish for $\tau = 0^\circ$ and are symmetric for $\pm\tau$, as required by the symmetry of the model.

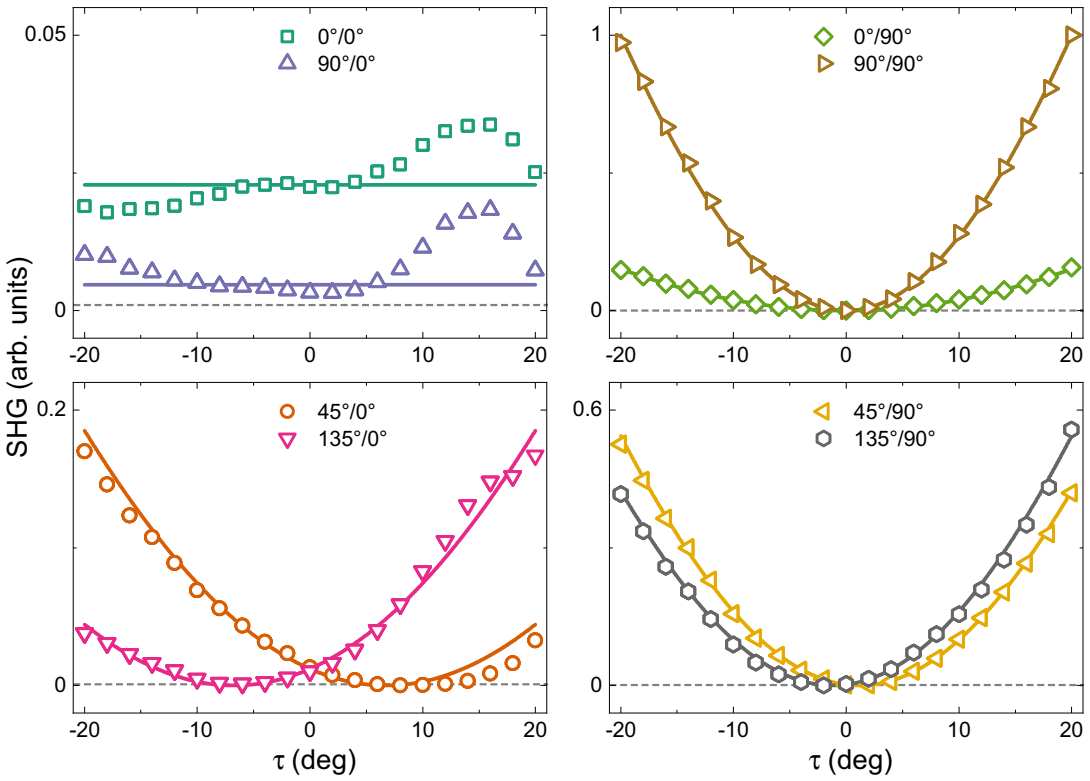

FIG. 4. SHG intensity for different polarization configurations for the multidomain PZT film, using the labeling introduced in Fig. 1, is shown as a function of the sample-rotation angle τ. The data are grouped such that the $\alpha^{\omega}_{\text{in}}/0^{\circ}$ and $\alpha^{\omega}_{\text{in}}/\ 90^{\circ}$ configurations are shown in the left and right column, respectively. The top (bottom) row is characterized by $\alpha^{\omega}_{\text{in}} = 0^{\circ}, 90^{\circ}$ ($\alpha^{\omega}_{\text{in}} = 45^{\circ}, 135^{\circ}$). Data are normalized to the $90^{\circ}/90^{\circ}$ configuration at $\tau = 20^{\circ}$. The dashed lines indicate the instrumental background. Continuous lines correspond to the fit model of Eqs. (4.5) and (4.6) with all data fitted with one set of parameters (Table I). The multidomain sample is characterized by a small but nonzero signal for the $0\,^{\circ}/0\,^{\circ}$ configuration (top-left panel), which certifies the presence of a_2 domains as detailed in the main text. Data acquisition of the small SHG signals obtained in the $\alpha^{\omega}_{\text{in}}/0^{\circ}$ configurations is dominated by systematic variations due to a background-signal drift occurring as a function of measurement time. Note that the $45^{\circ}/\alpha^{2\omega}_{\text{out}}$ and $135^{\circ}/\alpha^{2\omega}_{\text{out}}$ configurations (bottom row) are no longer symmetric for $\pm\tau$, as expected by the breaking of the model symmetry induced by the presence of a_2 domains.

of the 75-nm PZT film [43]. The data collected for this sample together with the result of the fit of Eqs. (4.5) and (4.6) are shown in Fig. 4 and Table I. We find a nonzero SHG signal in the $0^{\circ}/0^{\circ}$ polarization configuration when $\tau = 0^{\circ}$. Due to the specific sample alignment ($[010]_{\text{PZT}}// y'$, as described in Fig. 1), this signal can solely be associated with the tensor component χ^{a2}_{yyy}, certifying the presence of a_2 domains in the sample. From the fit, we determine that the these domains are polarized along $[010]_{\text{PZT}}$ ($A^{a2+} = 4 \pm 1\%$) with a negligible number of oppositely polarized domains ($A^{a2-} \approx 0\%$) within the error of the fit. We also find a negligible number of orthogonally polarized domains ($A^{a1+} \sim A^{a1-} \approx 0\%$). Hence, from the fitted domain-area fractions (Table I), we conclude that the multidomain PZT sample is characterized by an a-c-domain configuration (Fig. 2). The imbalance in the distribution of the $\pm a_1/a_2$ is expected in PZT films grown on DSO. It is conventionally attributed to the combined influence of the anisotropic elastic modulus of the substrate and small tensile stress that favors the appearance of one in-plane domain orientation over the others [52,53].

Surprisingly, we find that the ratios between the independent components of χ^{c}_{ijk} are different between the 15-nm and 75-nm samples. In particular, the χ^{c}_{zxx} component is more than double in the multidomain sample while the χ^{c}_{xzx} components are comparable. A similar trend is observed for the in-plane domains with the χ^{a2}_{yzz} tensor component (χ^{v}_{zxx} in the local coordinate system), nearly doubling the multidomain χ^{c}_{zxx} value, whereas the χ^{a2}_{zyz} (χ^{v}_{xzx} in the local coordinate system) is comparable with χ^{c}_{xzx}. By neglecting the 75-nm-thick-film birefringence, we are introducing an error with an upper limit of 0.5%, therefore this variation must have a different origin. It has been suggested that the magnitude of the $\hat{\chi}^{(2)}$ tensor components is modulated by strain via coupling with the nonlinear photoelastic tensor [54]. Indeed, the strain-induced modification of the nonlinear susceptibility tensor due to a photoelastic effect has been exploited to determine both the strain and the photoelastic tensor elements in two-dimensional MoS_2 via SHG anisotropy measurements [55]. Therefore, it is plausible to assume that ferroelectric domains subjected to different epitaxial strain conditions will be characterized by different values of the χ^{v}_{ijk} component ratios. Even without explicitly introducing the nonlinear photoelastic tensor to our model, this appears to be the case of our films, as in the a-c-domain configuration of the multidomain PZT film the stripe-shaped a domains and also the c-domain matrix are subjected to a different local strain state when compared to

TABLE I. Determination of the χ_{ijk} tensor-component ratios and of the relative domain fraction as derived from the SHG fit model described in Eqs. (4.3)–(4.6). For the labeling of the χ_{ijk} component ratios, we use a reduced notation where we incorporate Eqs. (3.2)–(3.4) expressed in tensor components using the global coordinate system of the crystal. For the single-domain sample, the tensor components of each single domain state have the same values in the local coordinate system. In the multidomain sample, the tensor components for in-plane (a_1, a_2) and out-of-plane (c) domains are allowed to have different values in the local coordinate system. Failure in doing so results in poor fit quality. Values $A^{\nu\pm}$ are the area fractions of the specific domain variant ν ($\nu = a_1$, a_2 and c). The values δA^{ν} represent the domain imbalance between oppositely polarized domains of a 180° pair as described in Eq. (4.7).

	Single domain	Multidomain
$\chi^{c}_{zxx}/\chi^{c}_{zzz}$	0.11 ± 0.01	0.28 ± 0.03
$\chi^{c}_{xzx}/\chi^{c}_{zzz}$	0.20 ± 0.01	0.22 ± 0.03
$\chi^{a2}_{yzz}/\chi^{a2}_{yyy}$	$= \chi^{c}_{zxx}/\chi^{c}_{zzz}$	0.49 ± 0.06
$\chi^{a2}_{zyz}/\chi^{a2}_{yyy}$	$= \chi^{c}_{xzx}/\chi^{c}_{zzz}$	0.27 ± 0.03
$\chi^{a1}_{xyy}/\chi^{a1}_{xxx}$	$= \chi^{c}_{zxx}/\chi^{c}_{zzz}$	$= \chi^{a2}_{yzz}/\chi^{a2}_{yyy}$
$\chi^{a1}_{yxy}/\chi^{a1}_{xxx}$	$= \chi^{c}_{xzx}/\chi^{c}_{zzz}$	$= \chi^{a2}_{zyz}/\chi^{a2}_{yyy}$
A^{a1+}	$0.3 \pm 1\%$	$0.3 \pm 1\%$
A^{a1-}	$0.1 \pm 1\%$	$0.3 \pm 1\%$
δA^{a1}	0%	0%
A^{a2+}	$0.1 \pm 1\%$	$4 \pm 1\%$
A^{a2-}	$0.2 \pm 1\%$	$0.1 \pm 1\%$
δA^{a2}	0%	$4 \pm 1\%$
A^{c+}	$99.5 \pm 0.5\%$	$95 \pm 4\%$
A^{c-}	$0.1 \pm 1\%$	$0.1 \pm 1\%$
δA^{c}	$99.5 \pm 0.5\%$	$95 \pm 4\%$

the fully-c-oriented PZT film [43,46]. Hence, the different strain state of the films is not only causing the emergence of distinct domain configurations, but in addition it modulates their local nonlinear response. Recent experiments performed on a $BaTiO_3$ thin film epitaxially grown onto a piezoelectric substrate indicate that the SHG signal produced in the ferroelectric layer can be *operando* modulated via the strain induced by the inverse piezoelectric effect of the substrate, further corroborating our hypothesis [56].

VI. CONCLUSIONS

We have developed a model to quantify the distribution of a_1-, a_2-, and c-oriented domains in tetragonal ferroelectric thin films from SHG polarization anisotropy measurements using PZT as our prototype material. We first tested the validity of our approach on a single-c-domain film, and we find that our model provides a good fit to the experimental data. We then expanded our model towards the analysis of multidomain films and the extraction of their specific domain configuration. Following this procedure, we determined that our epitaxially engineered multidomain PZT model film is characterized by an a-c-domain configuration with a_2 domains distributed within a c-domain environment. We also found that the strain resulting from both the epitaxy and the multidomain configuration itself has significant influence on the nonlinear susceptibilities.

We now have SHG as a tool for quantifying domain distributions in tetragonal ferroelectrics with, in principle, arbitrary domain architectures. The capability of SHG of discriminating the different nonlinear contributions associated to specific domain configurations is crucial for the characterization of complex ferroelectric domain arrangements. The noninvasiveness of the SHG experiment allows for *in situ* and *operando* characterizations. The spatial resolution can be employed to resolve domain architectures, while the temporal resolution down to femtosecond scale enables studies of their dynamical properties. We are confident that this paper will stimulate further investigations on the topology of the domain distributions in nanoscale ferroelectric thin films and their analysis performed with nonlinear optical methods.

ACKNOWLEDGMENTS

This research was supported by Swiss National Science Foundation Project No. 200021_178825. The authors thank Thomas Lottermoser for the stimulating discussions held during the development of the SHG model. G.D.L. thanks Morgan Trassin for the experimental support provided during the thin-film growth.

[1] M. E. Lines and A. M. Glass, *Principles and Applications of Ferroelectrics and Related Materials* (Clarendon, Oxford, 2001).

[2] J. F. Scott, Applications of modern ferroelectrics, Science **315**, 954 (2007).

[3] L. W. Martin and A. M. Rappe, Thin-film ferroelectric materials and their applications, Nat. Rev. Mater. **2**, 16087 (2016).

[4] H. Kohlstedt, Y. Mustafa, A. Gerber, A. Petraru, M. Fitsilis, R. Meyer, U. Böttger, and R. Waser, Current status and challenges of ferroelectric memory devices, Microelectron. Eng. **80**, 296 (2005).

[5] N. A. Spaldin and R. Ramesh, Advances in magnetoelectric multiferroics, Nat. Mater. **18**, 203 (2019).

[6] E. Soergel, Piezoresponse force microscopy (PFM), J. Phys. D **44**, 464003 (2011).

[7] A. Gruverman, M. Alexe, and D. Meier, Piezoresponse force microscopy and nanoferroic phenomena, Nat. Commun. **10**, 1 (2019).

[8] Y. Mi, G. Geneste, J. E. Rault, C. Mathieu, A. Pancotti, and N. Barrett, Polarization dependent chemistry of ferroelectric $BaTiO_3$ (001) domains, J. Phys.: Condens. Matter **24**, 275901 (2012).

[9] K. A. Hunnestad, E. D. Roede, A. T. J. Van Helvoort, and D. Meier, Characterization of ferroelectric domain walls by scanning electron microscopy, J. Appl. Phys. **128**, 191102 (2020).

[10] J. T. Heron, J. L. Bosse, Q. He, Y. Gao, M. Trassin, L. Ye, J. D. Clarkson, C. Wang, J. Liu, S. Salahuddin, D. C. Ralph,

D. G. Schlom, J. Íñiguez, B. D. Huey, and R. Ramesh, Deterministic switching of ferromagnetism at room temperature using an electric field, Nature (London) **516**, 370 (2014).

[11] T. H. E. Lahtinen, J. O. Tuomi, and S. van Dijken, Pattern transfer and electric-field-induced magnetic domain formation in multiferroic heterostructures, Adv. Mater. **23**, 3187 (2011).

[12] J. Nordlander, G. De Luca, N. Strkalj, M. Fiebig, and M. Trassin, Probing ferroic states in oxide thin films using optical second harmonic generation, Appl. Sci. **8**, 570 (2018).

[13] G. De Luca, N. Strkalj, S. Manz, C. Bouillet, M. Fiebig, and M. Trassin, Nanoscale design of polarization in ultrathin ferroelectric heterostructures, Nat. Commun. **8**, 1419 (2017).

[14] F. Lyzwa, P. Marsik, V. Roddatis, C. Bernhard, M. Jungbauer, and V. Moshnyaga, *In situ* monitoring of atomic layer epitaxy via optical ellipsometry, J. Phys. D **51**, 125306 (2018).

[15] A. Fluri, D. Pergolesi, V. Roddatis, A. Wokaun, and T. Lippert, *In situ* stress observation in oxide films and how tensile stress influences oxygen ion conduction, Nat. Commun. **7**, 10692 (2016).

[16] V. Gopalan and R. Raj, Electric field induced domain rearrangement in potassium niobate thin films studied by in situ second harmonic generation measurements, J. Appl. Phys. **81**, 865 (1997).

[17] C. Canalias, V. Pasiskevicius, F. Laurell, S. Grilli, P. Ferraro, and P. De Natale, *In situ* visualization of domain kinetics in flux grown $KTiOPO_4$ by digital holography, J. Appl. Phys. **102**, 064105 (2007).

[18] G. De Luca, P. Schoenherr, J. Mendil, D. Meier, M. Fiebig, and M. Trassin, Domain-pattern transfer across an artificial magnetoelectric interface, Phys. Rev. Appl. **10**, 054030 (2018).

[19] S. E. Cummins and T. E. Luke, A new method of optically reading domains in bismuth titanate for display and memory applications, IEEE Trans. Electron Devices **18**, 761 (1971).

[20] Y. Uemura, S. Matsuoka, J. Tsutsumi, S. Horiuchi, S. Arai, and T. Hasegawa, Birefringent field-modulation imaging of transparent ferroelectrics, Phys. Rev. Appl. **14**, 024060 (2020).

[21] D. A. Tenne, A. Bruchhausen, N. D. Lanzillotti-Kimura, A. Fainstein, R. S. Katiyar, A. Cantarero, A. Soukiassian, V. Vaithyanathan, J. H. Haeni, W. Tian, D. G. Schlom, K. J. Choi, D. M. Kim, C. B. Eom, H. P. Sun, X. Q. Pan, Y. L. Li, L. Q. Chen, Q. X. Jia, S. M. Nakhmanson, K. M. Rabe, and X. X. Xi, Probing nanoscale ferroelectricity by ultraviolet raman spectroscopy, Science **313**, 1614 (2006).

[22] J. Kreisel, M. C. Weber, N. Dix, F. Sánchez, P. A. Thomas, and J. Fontcuberta, Probing individual layers in functional oxide multilayers by wavelength-dependent Raman scattering, Adv. Funct. Mater. **22**, 5044 (2012).

[23] S. A. Denev, T. T. A. Lummen, E. Barnes, A. Kumar, and V. Gopalan, Probing ferroelectrics using optical second harmonic generation, J. Am. Ceram. Soc. **94**, 2699 (2011).

[24] R. C. Miller, Optical harmonic generation in single crystal $BaTiO_3$, Phys. Rev. **134**, A1313 (1964).

[25] T. H. Maiman, Stimulated optical radiation in ruby, Nature (London) **187**, 493 (1960).

[26] V. Gopalan and R. Raj, Domain structure-second harmonic generation correlation in potassium niobate thin films deposited on a strontium titanate substrate, J. Am. Ceram. Soc. **79**, 3289 (1996).

[27] Y. Barad, J. Lettieri, C. D. Theis, D. G. Schlom, V. Gopalan, J. C. Jiang, and X. Q. Pan, Probing domain microstructure in ferroelectric $Bi_4Ti_3O_{12}$ thin films by optical second harmonic generation, J. Appl. Phys. **89**, 1387 (2001).

[28] K. J. Choi, M. Biegalski, Y. L. Li, A. Sharan, J. Schubert, R. Uecker, P. Reiche, Y. B. Chen, X. Q. Pan, V. Gopalan, L.-Q. Chen, D. G. Schlom, and C. B. Eom, Enhancement of ferroelectricity in strained $BaTiO_3$ thin films, Science **306**, 1005 (2004).

[29] Y. L. Li, S. Choudhury, J. H. Haeni, M. D. Biegalski, A. Vasudevarao, A. Sharan, H. Z. Ma, J. Levy, V. Gopalan, S. Trolier-McKinstry, D. G. Schlom, Q. X. Jia, and L. Q. Chen, Phase transitions and domain structures in strained pseudocubic (100) $SrTiO_3$ thin films, Phys. Rev. B **73**, 184112 (2006).

[30] R. J. Zeches, M. D. Rossell, J. X. Zhang, A. J. Hatt, Q. He, C.-H. Yang, A. Kumar, C. H. Wang, A. Melville, C. Adamo, G. Sheng, Y.-H. Chu, J. F. Ihlefeld, R. Erni, C. Ederer, V. Gopalan, L.-Q. Q. Chen, D. G. Schlom, N. A. Spaldin, L. W. Martin, and R. Ramesh, A strain-driven morphotropic phase boundary in $BiFeO_3$, Science **326**, 977 (2009).

[31] R. Zu, B. Wang, J. He, J. J. Wang, L. Weber, L. Q. Chen, and V. Gopalan, Analytical and numerical modeling of optical second harmonic generation in anisotropic crystals using ♯SHAARP package, npj Comput. Mater. **8**, 246 (2022).

[32] R. W. Boyd, *Nonlinear Optics* (Academic, New York, 2008).

[33] M. Fiebig, V. V. Pavlov, and R. V. Pisarev, Second-harmonic generation as a tool for studying electronic and magnetic structures of crystals: Review, J. Opt. Soc. Am. B **22**, 96 (2005).

[34] V. K. Wadhawan, *Introduction to Ferroic Materials* (Gordon and Breach, New York, 2000).

[35] M. Acosta, N. Novak, V. Rojas, S. Patel, R. Vaish, J. Koruza, G. A. Rossetti, and J. Rödel, $BaTiO_3$-based piezoelectrics: Fundamentals, current status, and perspectives, Appl. Phys. Rev. **4**, 041305 (2017).

[36] P. K. Panda and B. Sahoo, PZT to lead free piezo ceramics: A review, Ferroelectrics **474**, 128 (2015).

[37] J. Wu, D. Xiao, and J. Zhu, Potassium-sodium niobate lead-free piezoelectric materials: Past, present, and future of phase boundaries, Chem. Rev. **115**, 2559 (2015).

[38] R. R. Neurgaonkar, W. F. Hall, J. R. Oliver, W. W. Ho, and W. K. Cory, Tungsten bronze $Sr_{1-x}Ba_xNb_2O_6$: A case history of versatility, Ferroelectrics **87**, 167 (1988).

[39] R. R. Birss, *Symmetry and Magnetism* (North-Holland, Amsterdam, 1964).

[40] J. Kaneshiro, Y. Uesu, and T. Fukui, Visibility of inverted domain structures using the second harmonic generation microscope: Comparison of interference and non-interference cases, J. Opt. Soc. Am. B **27**, 888 (2010).

[41] A. L. Roytburd, J. Ouyang, and A. Artemev, Polydomain structures in ferroelectric and ferroelastic epitaxial films, J. Phys. Condens. Matter **29**, 163001 (2017).

[42] D. Fröhlich, T. Kiefer, S. Leute, and T. Lottermoser, Nonlinear spectroscopy of antiferromagnetics, Appl. Phys. B **68**, 465 (1999).

[43] G. De Luca, M. D. Rossell, J. Schaab, N. Viart, M. Fiebig, and M. Trassin, Domain wall architecture in tetragonal ferroelectric thin films, Adv. Mater. **29**, 1605145 (2017).

[44] D. Zekria, A. M. Glazer, V. Shuvaeva, J. Dec, and S. Miga, Birefringence of lead titanate ($PbTiO_3$), J. Appl. Crystallogr. **37**, 551 (2004).

[45] A. Schilling, T. B. Adams, R. M. Bowman, J. M. Gregg, G. Catalan, and J. F. Scott, Scaling of domain periodicity with

thickness measured in $BaTiO_3$ single crystal lamellae and comparison with other ferroics, Phys. Rev. B **74**, 024115 (2006).

[46] L. Feigl, P. Yudin, I. Stolichnov, T. Sluka, K. Shapovalov, M. Mtebwa, C. S. Sandu, X.-K. Wei, A. K. Tagantsev, and N. Setter, Controlled stripes of ultrafine ferroelectric domains, Nat. Commun. **5**, 4677 (2014).

[47] C. W. van Hasselt, M. A. C. Devillers, T. Rasing, and O. A. Aktsipetrov, Second-harmonic generation from thick thermal oxides on Si(111): The influence of multiple reflections, J. Opt. Soc. Am. B **12**, 33 (1995).

[48] M.-Z. Huang and W. Y. Ching, Calculation of optical excitations in cubic semiconductors. II. Second-harmonic generation, Phys. Rev. B **47**, 9464 (1993).

[49] E. D. Mishina, N. E. Sherstyuk, A. V. Mishina, V. M. Mukhorotov, G. Buinutskaya, L. L. Kulyuk, and T. Rasing, Optical second harmonic generation for determination the domain orientation in thin ferroelectric films, Ferroelectrics **286**, 279 (2003).

[50] I. Shoji, T. Kondo, A. Kitamoto, M. Shirane, and R. Ito, Absolute scale of second-order nonlinear-optical coefficients, J. Opt. Soc. Am. B **14**, 2268 (1997).

[51] S. M. Anderson and B. S. Mendoza, Three-layer model for the surface second-harmonic generation yield including multiple reflections, Phys. Rev. B **94**, 115314 (2016).

[52] O. Nesterov, S. Matzen, C. Magen, a. H. G. Vlooswijk, G. Catalan, and B. Noheda, Thickness scaling of ferroelastic domains in $PbTiO_3$ films on $DyScO_3$, Appl. Phys. Lett. **103**, 142901 (2013).

[53] L. Feigl, L. J. McGilly, C. S. Sandu, and N. Setter, Compliant ferroelastic domains in epitaxial Pb(Zr, Ti)O_3 thin films, Appl. Phys. Lett. **104**, 172904 (2014).

[54] J.-W. Jeong, S.-C. Shin, I. L. Lyubchanskii, and V. N. Varyukhin, Strain-induced three-photon effects, Phys. Rev. B **62**, 13455 (2000).

[55] L. Mennel, M. M. Furchi, S. Wachter, M. Paur, D. K. Polyushkin, and T. Mueller, Optical imaging of strain in two-dimensional crystals, Nat. Commun. **9**, 516 (2018).

[56] K. J. Kormondy, Y. Cho, A. B. Posadas, L. Zheng, K. Lai, Q. Wang, M. J. Kim, Q. He, A. Y. Borisevich, M. C. Downer, and A. A. Demkov, Piezoelectric modulation of nonlinear optical response in $BaTiO_3$ thin film, Appl. Phys. Lett. **113**, 132902 (2018).